nature COMMUNICATIONS

ARTICLE

https://doi.org/10.1038/s41467-020-16715-6 OPEN

Nanocasting SiO_2 into metal–organic frameworks imparts dual protection to high-loading Fe single-atom electrocatalysts

Long Jiao[1,6], Rui Zhang[1,6], Gang Wan[2,6], Weijie Yang[3], Xin Wan[4], Hua Zhou[5], Jianglan Shui[4], Shu-Hong Yu[1] & Hai-Long Jiang[1✉]

Single-atom catalysts (SACs) have sparked broad interest recently while the low metal loading poses a big challenge for further applications. Herein, a dual protection strategy has been developed to give high-content SACs by nanocasting SiO_2 into porphyrinic metal–organic frameworks (MOFs). The pyrolysis of SiO_2@MOF composite affords single-atom Fe implanted N-doped porous carbon (Fe_{SA}–N–C) with high Fe loading (3.46 wt%). The spatial isolation of Fe atoms centered in porphyrin linkers of MOF sets the first protective barrier to inhibit the Fe agglomeration during pyrolysis. The SiO_2 in MOF provides additional protection by creating thermally stable FeN_4/SiO_2 interfaces. Thanks to the high-density Fe_{SA} sites, Fe_{SA}–N–C demonstrates excellent oxygen reduction performance in both alkaline and acidic medias. Meanwhile, Fe_{SA}–N–C also exhibits encouraging performance in proton exchange membrane fuel cell, demonstrating great potential for practical application. More far-reaching, this work grants a general synthetic methodology toward high-content SACs (such as Fe_{SA}, Co_{SA}, Ni_{SA}).

[1] Hefei National Laboratory for Physical Sciences at the Microscale, CAS Key Laboratory of Soft Matter Chemistry, Collaborative Innovation Center of Suzhou Nano Science and Technology, Department of Chemistry, University of Science and Technology of China, Hefei, Anhui 230026, People's Republic of China. [2] Materials Science Division, Argonne National Laboratory, Lemont, IL 60439, USA. [3] School of Energy and Power Engineering, North China Electric Power University, Baoding 071003, People's Republic of China. [4] School of Materials Science and Engineering, Beihang University, Beijing 100083, People's Republic of China. [5] X-ray Science Division, Advanced Photon Source, Argonne National Laboratory, Lemont, IL 60439, USA. [6] These authors contributed equally: Long Jiao, Rui Zhang, Gang Wan. ✉email: jianglab@ustc.edu.cn

Single-atom catalysts (SACs), with the maximal utilization of metal atoms, open up a new frontier and attract increasing attention in catalysis[1–10]. Integrated with plenty of merits, including highly dispersed sites, high activity, excellent selectivity, and good reusability, SACs have been regarded as an ideal platform to bridge the gap between homogenous and heterogeneous catalysts[1–4]. Nevertheless, isolated metal atoms in SACs tend to agglomerate due to the high surface energy. Though significant progress has been achieved to ensure the atomic dispersion of metal atoms, metal loadings of SACs are basically low (<1 wt%). The construction methodology of stable SACs, especially in high metal loadings, is highly desired yet remains a grand challenge[11–13]. In addition, to boost the catalytic performance of SACs, their physical features, including porous structure and surface area, which dominate the accessibility to active sites, should also be optimized[14–16].

Metal–organic frameworks (MOFs)[17–25], featuring well-defined and tailored structures, present particular advantages in the precise fabrication of catalysts, especially SACs[26–33]. The present synthetic strategy for MOF-based SACs is to augment the distance between adjacent metal atoms based on the mixed metal/ligand and pore confinement, which effectively inhibits the agglomeration of metal atoms under pyrolysis[27–30]. Unfortunately, these strategies cause the decrease of metal loadings. As a result, even bearing the structural advantages in MOF-based SACs, their metal loadings are unsatisfying, such as Fe_{SA} (usually, <2 wt%)[26–33]. In addition, most of reported MOF-derived SACs possess micropores (<2 nm), which is unfavorable to mass transfer in catalytic process[27,30]. To address these issues, alternative synthetic strategies for MOF-derived SACs are imperative to improving the metal loadings and pore structures.

To realize SACs with high metal loadings, the main obstacle to overcome is their easy-to-migrate feature due to their high surface energy, especially under pyrolysis. It was found that inorganic silica (SiO_2) protection method can stabilize metal nanoparticles/clusters by decreasing surface energy of metal atoms[1,34–38], which might be effective toward the stabilization of highly loaded SACs. Making full use of the porosity of MOFs, SiO_2 can be easily nanocasted into the pore space of MOFs to interact with the isolated metal atoms on MOF skeleton, which would significantly lower their surface energy. In consequence, the introduction of SiO_2 into MOFs, when integrated with the merits of MOFs, should be a very promising route to improve metal loadings in SACs.

In this work, we creatively put forward a nanocasting strategy to introduce SiO_2 into the mesopores of a porphyrinic MOF, PCN-222(Fe), featuring single Fe(III) site in each porphyrin linker[39–41]. Thanks to the 1D mesochannel with a diameter of ~3.2 nm, SiO_2 can be sufficiently filled into PCN-222(Fe), forming thermal stable FeN_4/SiO_2 interfaces. Upon high-temperature pyrolysis and SiO_2 removal, the single-atom Fe catalyst, denoted Fe_{SA}–N–C, with a Fe loading as high as 3.46 wt%, is obtained (Fig. 1). During the pyrolysis, the spatial isolation of Fe atoms anchored by N atoms in porphyrin linkers is the first protective barrier to inhibit the Fe agglomeration. The silica in MOF channels serves as oxide substrate to interact with Fe atoms that can increase migration energy barrier of Fe atoms and prevent their aggregation. Meanwhile, upon removal of silica, the porosity and surface area of the resultant N-doped porous carbon can be improved, benefiting the exposure of active sites and mass transfer. As a result, the optimized Fe_{SA}–N–C exhibits excellent oxygen reduction reaction (ORR) performance, surpassing the state-of-the-art Pt/C, and almost all reported non-noble-metal catalysts, in both alkaline and the more challenging acidic solutions. Significantly, the Fe_{SA}–N–C reaches a current density of 292 mA cm^{-2} at 0.8 V and the highest power density of 0.68 W cm^{-2}, comparable to that of the best non-noble metal catalysts, in H_2–O_2 proton exchange membrane fuel cell (PEMFC).

Results

Synthesis and characterization of Fe_{SA}–N–C. The PCN-222(Fe) was prepared by employing trifluoroacetic acid (TFA), instead of the traditionally used benzoic acid, as a modulator (Supplementary Fig. 1)[39]. The scanning electron microscopy (SEM) image of PCN-222(Fe) presents the uniform spindle morphology with a diameter ~250 nm (Fig. 2a). The low boiling point of TFA makes it easy to be removed by direct degassing without additional pre-activation process (necessary for benzoic acid modulator) to deliver available pore space in PCN-222(Fe) (Supplementary Table 1). The N_2 sorption with a typical type-IV isotherms present a high surface area up to 2040 m^2 g^{-1} and the pore size distribution suggests the mesochannels centered at 3.2 nm, in good agreement with the transmission electron microscopy (TEM) observation (Fig. 2b, Supplementary Fig. 2). This greatly facilitates the subsequent introduction of tetraethylorthosilicate (TEOS) into PCN-222(Fe) mesopores for SiO_2 nanocasting, after degassing the MOF at 150 °C. The facile TFA removal and mesoporosity guarantee the sufficient percolation of TEOS through the entire inner space of PCN-222(Fe). Upon HCl vapor treatment, TEOS in PCN-222(Fe) can be hydrolyzed and condensed to silica, affording SiO_2@PCN-222(Fe) composite with well-retained MOF crystallinity, thanks to the ultrahigh acidic stability of the MOF (Supplementary Fig. 1)[39].

The infrared peak at 1090 cm^{-1} assignable to Si-O-Si clearly confirms the SiO_2 formation (Supplementary Fig. 3)[37]. The reduced surface area (1190 m^2 g^{-1}) and mesopore size (2.9 nm) in the composite, in reference to the parent MOF (BET of 2040 m^2 g^{-1}; pore size of 3.2 nm), further indicate the successful infiltration of SiO_2 in PCN-222(Fe). The elemental mapping images of SiO_2@PCN-222(Fe) further illustrate the homogeneous dispersion of Si in PCN-222(Fe) (Supplementary Fig. 4). After the pyrolysis of SiO_2@PCN-222(Fe) at 800 °C, the composite of metal (oxides) stabilized by porous carbon is produced. Upon the removal of the oxide by acid etching, Fe_{SA}–N–C with retained spindle morphology is finally obtained and no particles are observed in TEM images (Fig. 2c–e, Supplementary Fig. 5a). The elemental mapping images clearly demonstrate the homogenous dispersion of Fe and N elements on Fe_{SA}–N–C (Supplementary Fig. 6). Aberration-corrected high-angle annular darkfield scanning transmission electron microscope (HAADF-STEM) observation shows the isolated and high-density bright spots, implying the formation of single metal atoms (Fig. 2f, Supplementary Fig. 5b). The accurate contents of Fe (3.46 wt%) and N (4.87 wt%) have been quantified by inductively coupled plasma atomic emission spectrometry (ICP) and elemental analysis, demonstrating the presence of single Fe atom and suggesting the higher Fe loading than almost all reported single-atom Fe-incorporated carbon-based materials (Supplementary Table 2). Moreover, the quantitative analysis of X-ray photoelectron spectroscopy (XPS) and energy-dispersive spectroscopy further confirm the high loading of Fe, in accordance with the ICP results (Supplementary Table 3). In addition, the content of Zr is extremely low, illustrating Fe is the dominated metal species in Fe_{SA}–N–C (Supplementary Table 3). As illustrated above, the perfect combination of PCN-222(Fe) and SiO_2 can exert their respective advantages for the creation of the resultant Fe_{SA}–N–C, which are visually summarized (Supplementary Fig. 7).

Powder X-ray diffraction (PXRD) pattern of Fe_{SA}–N–C gives two broad peaks in the ranges of 20–30° and 40–45°, corresponding to (002) and (101) planes of graphitized carbon, and no diffraction of Fe-based species is identifiable, in

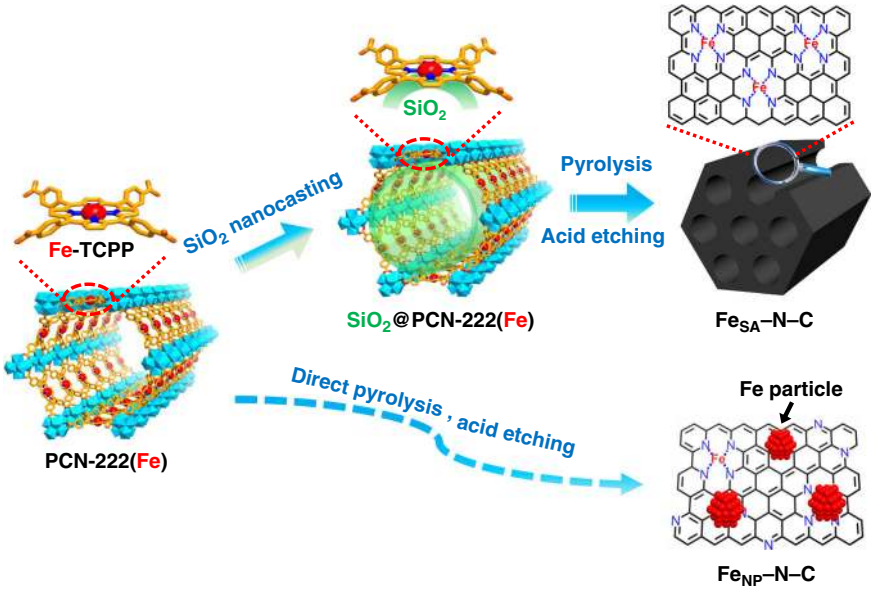

Fig. 1 Schematic illustration. Illustration showing the nanocasting-assisted fabrication of Fe_{SA}-N-C from PCN-222(Fe).

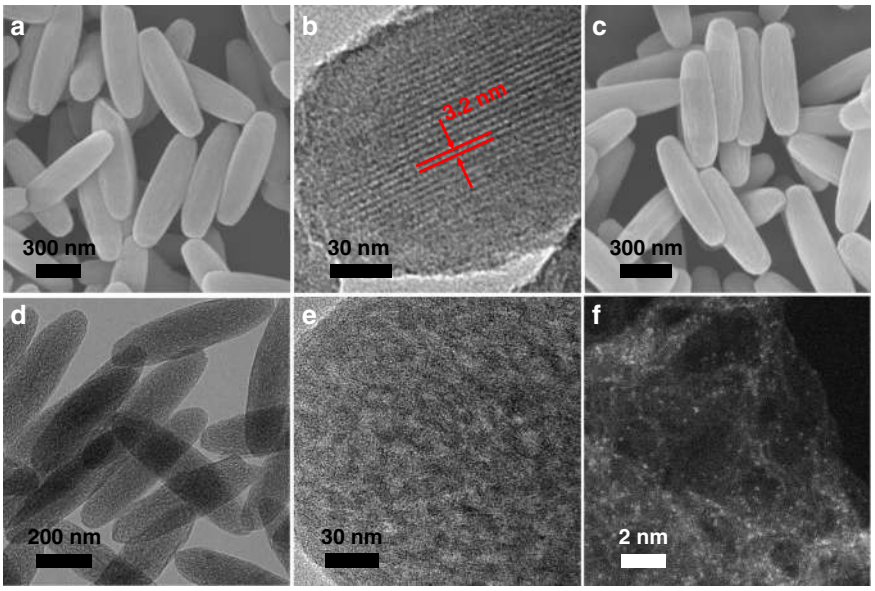

Fig. 2 Microscopic characterizations. a Scanning electron microscopy (SEM) and **b** transmission electron microscopy (TEM) images of PCN-222(Fe). **c** SEM and **d** TEM images of Fe_{SA}-N-C. **e** Enlarged TEM image showing the mesoporous structure of Fe_{SA}-N-C. **f** Aberration-corrected HAADF-STEM image of Fe_{SA}-N-C.

accordance with the TEM observation results (Fig. 2c–e, Supplementary Fig. 8). Raman scattering spectrum for Fe_{SA}–N–C gives low intensity ratio ($I_D/I_G = 0.95$) of D band (~1345 cm^{-1}) and G band (~1590 cm^{-1}), illustrating the high graphitization degree (Supplementary Fig. 9). N_2 sorption measurement for Fe_{SA}–N–C manifests its high BET surface area up to 1615 $m^2 g^{-1}$ (Supplementary Fig. 10). The mesoporous pore size distribution extends up to 10 nm (Supplementary Fig. 10), which can be also seen in enlarged TEM image (Fig. 2e). The large surface area and hierarchical pore of Fe_{SA}–N–C would make the single Fe atoms readily accessible and guarantee high-flux mass transfer, which are essential to boost the catalysis[42]. The existing states of Fe and N elements have been examined by XPS. The N 1 s XPS spectrum of Fe_{SA}–N–C is fitted into five configurations, including pyridinic N (398.5 eV), Fe–N (399.2 eV), pyrrolic N (400.2 eV), graphitic N (401.1 eV), and oxidized N (402.9 eV), respectively (Supplementary Fig. 11a)[27–29,34–38,43]. The Fe 2 $p_{3/2}$ binding energy in Fe_{SA}–N–C centers at 710.5 eV (close to Fe^{3+}), suggesting the positively charged Fe atoms (Supplementary Fig. 11b). No Fe^0 belonging to Fe particle can be identified from XPS spectrum, in consistent with the absence of Fe particles from PXRD and TEM results (Fig. 2d–f, Supplementary Fig. 8). In addition, no obvious Si residual can be detected from the XPS result of Fe_{SA}–N–C (Supplementary Fig. 12). It is noteworthy that the direct pyrolysis of PCN-222(Fe) without SiO_2 leads to the formation of Fe nanoparticles in the resultant catalyst (denoted Fe_{NP}–N–C), manifesting the important role of SiO_2 in inhibiting the agglomeration of Fe atoms under pyrolysis (Supplementary Fig. 13). The absence of Fe peaks in the XRD pattern of Fe_{NP}–N–C should be due to the small amount of Fe NPs (Supplementary Fig. 8).

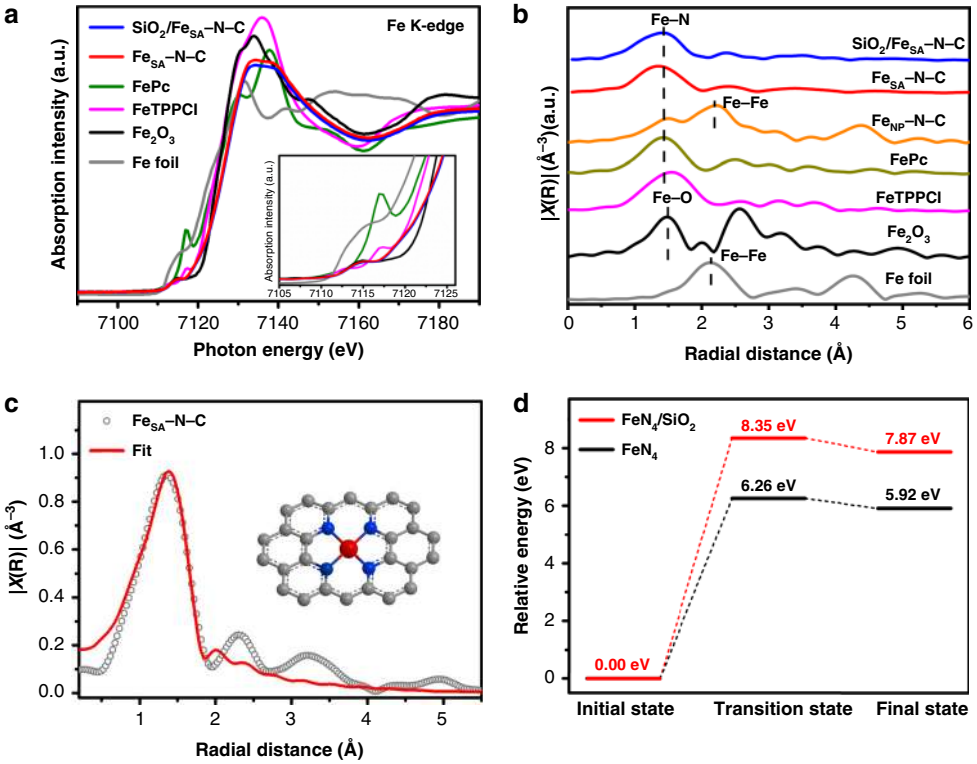

Fig. 3 Structure characterizations and DFT calculations. a Fe K-edge XANES and **b** FT-EXAFS spectra of SiO_2/Fe_{SA}–N–C, Fe_{SA}–N–C, and Fe_{NP}–N–C (represented by blue, red, and orange lines, respectively). **c** EXAFS fitting for Fe_{SA}–N–C (red line: fitting curve; gray cycles: experimental data). Inset: schematic model of Fe coordination environment in Fe_{SA}–N–C. The red, blue, and gray spheres represent Fe, N, and C atoms, respectively. **d** The relative energy along the intrinsic reaction coordinate for FeN_4/SiO_2 (red line) and FeN_4 (black line) migrating from initial state to final state.

X-ray absorption spectroscopy studies. To gain more information of the electronic structure and coordination environment of single Fe atoms in Fe_{SA}–N–C, X-ray absorption near-edge structure (XANES) and Fourier transform-extended X-ray absorption fine structure (FT-EXAFS) spectra have been examined. The XANES spectra of Fe in SiO_2/Fe_{SA}–N–C and Fe_{SA}–N–C show almost the same absorption edge located at between Fe foil and Fe_2O_3 (Fig. 3a), illustrating the positive valence state of Fe close to +3. The Fourier transformed EXAFS spectra of both SiO_2/Fe_{SA}–N–C and Fe_{SA}–N–C present a dominated peak at ~1.4 Å respecting to the Fe–N scattering path, and no Fe–Fe bond is detected (Fig. 3b). Furthermore, the curve fitting for EXAFS data of Fe_{SA}–N–C further verifies the coordination structure around Fe centers. The best fitting result for the first shell indicates that Fe atoms are fourfold coordinated by N atoms in average (Fig. 3c, Supplementary Fig. 14, Supplementary Table 4).

Insight into the formation process of Fe_{SA}–N–C. To unveil the critical role of the SiO_2 nanocasting for the generation of atomically dispersed Fe in Fe_{SA}–N–C, as a control, pure PCN-222(Fe) without SiO_2 was directly pyrolyzed at 800 °C in N_2 atmosphere. The Fe-based particles with clear Fe–Fe bond are observed in the EXAFS spectrum of Fe_{NP}–N–C, in stark contrast to that of Fe_{SA}–N–C derived from SiO_2@PCN-222(Fe) (Fig. 3b). The results above unambiguously demonstrate the crucial role of SiO_2 in the prevention of Fe atom migration/growth at a high loading under pyrolysis. To further illustrate the stabilizing effect of SiO_2 for Fe atoms in SiO_2/Fe_{SA}–N–C, the energy changes along the intrinsic reaction coordinate were also investigated through density functional theory (DFT) calculation. By selecting the FeN_4 and FeN_4/SiO_2 as representative models for Fe_{SA}–N–C and SiO_2/Fe_{SA}–N–C, respectively, the migration energies of each model from the initial state to the final state have been studied in detail (Supplementary Figs. 15–17). The migration energy barrier of Fe atom in FeN_4/SiO_2 is found to be 8.35 eV, obviously larger than 6.26 eV of FeN_4 without SiO_2, suggesting the more thermally stable Fe atoms in SiO_2/Fe_{SA}–N–C due to the stabilization effect of SiO_2 for Fe atoms (Fig. 3d). Moreover, SiO_2 also serves as a hard template, creating much larger surface area of Fe_{SA}–N–C (1615 $m^2 g^{-1}$) than those of Fe_{NP}–N–C (445 $m^2 g^{-1}$) and the N-doped porous carbon (simply as N–C, 612 $m^2 g^{-1}$) derived by the pyrolysis of PCN-222 without Fe centers (Supplementary Fig. 10). Therefore, the SiO_2-assisted MOF pyrolysis strategy is able to control the dispersion of active sites and tailor the microstructure of Fe_{SA}–N–C, which would be of great significance for subsequent catalysis.

Based on the results above, the formation process of Fe_{SA}–N–C from SiO_2@PCN-222(Fe) is readily understood. The periodic array of porphyrin linkers in the MOF guarantees the Fe isolation. The N atoms in porphyrin linker serve as the first safeguard to stabilize the Fe species. Moreover, the SiO_2 in the MOF pores behaves as an oxide support to further offer anchoring effect, upraising migration energy barrier of Fe atoms, and preventing their migration/growth upon pyrolysis (Fig. 3d). Based on the synergistic interactions endowed by the MOF and SiO_2, the thermal agglomeration of Fe atoms is suppressed, leading to the high Fe loadings in atomically dispersed form in Fe_{SA}–N–C. In addition to Fe_{SA}–N–C, Co_{SA}–N–C, and Ni_{SA}–N–C have also been successfully fabricated from SiO_2-nanocasted PCN-222(Co) and PCN-222(Ni), respectively, further manifesting the reliability and universality of this powerful strategy (Supplementary Fig. 18).

Electrocatalytic performance for ORR and fuel cells. Encouraged by the high-content single-atom Fe sites and pore structure

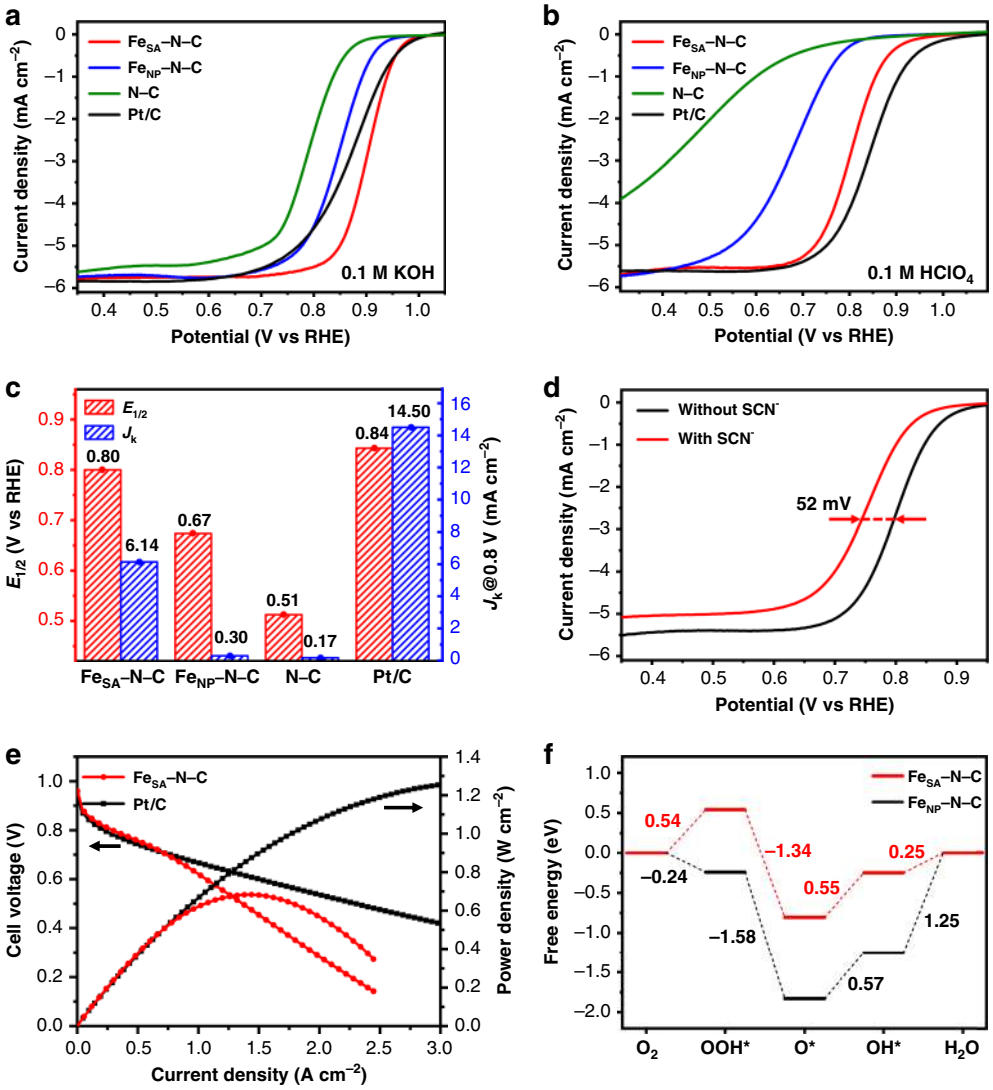

Fig. 4 Electrochemical performances and DFT calculations. LSV curves for Fe_{SA}-N-C (red line), Fe_{NP}-N-C (blue line), N-C (olive line) and Pt/C (black line) in **a** 0.1 M KOH and **b** 0.1 M $HClO_4$. **c** Comparison of $E_{1/2}$ and J_k at 0.80 V for various catalysts in 0.1 M $HClO_4$. **d** LSV curves of Fe_{SA}-N-C in 0.1 M $HClO_4$ before (black line) and after (red line) the addition of SCN^-. **e** Polarization and power density curves of PEMFCs with Fe_{SA}-N-C (red dots) and Pt/C (black dots) cathode catalysts. **f** Free energy diagrams of ORR on Fe_{SA}-N-C (red line) and Fe_{NP}-N-C (black line) in acidic media (pH = 1).

of Fe_{SA}–N–C, its ORR performance has been investigated. To our delight, when firstly tested in 0.1 M KOH solution, Fe_{SA}–N–C exhibits the highest half-wave potential ($E_{1/2}$ = 0.90 V) and kinetic current density (J_k) at 0.85 V (37.19 mA cm^{-2}) among Fe_{NP}–N–C, N–C and the commercial Pt/C. The mass activity of Fe_{SA}–N–C is calculated to be 21.36 mA g^{-1} at 0.9 V, much better than Fe_{NP}–N–C and N–C counterparts (Supplementary Table 5). The ideal 4e^- transfer process, as well as the excellent durability and methanol tolerance of Fe_{SA}–N–C all manifest the superior performance to Pt/C and most non-noble metal catalysts ever reported under alkaline conditions (Fig. 4a, Supplementary Figs. 19–22, Supplementary Table 6). Encouraged by the excellent ORR performance of Fe_{SA}–N–C in alkaline media, we further explore its performance under more challenging acidic conditions. When tested in 0.1 M $HClO_4$, the linear sweep voltammetry (LSV) curve of Fe_{SA}–N–C shows remarkable ORR activity with much higher $E_{1/2}$ (0.80 V) than that of Fe_{NP}–N–C (0.67 V), and N–C (0.51 V; Fig. 4b, c). Also, Fe_{SA}–N–C shows better mass activity 1.12 mA g^{-1} at 0.9 V than that of Fe_{NP}–N–C and N–C counterparts (Supplementary Table 7). In addition, Fe_{SA}–N–C demonstrates superior J_k at 0.80 V (6.14 mA cm^{-2}) to that of Fe_{NP}–N–C (0.30 mA cm^{-2}) and N–C (0.17 mA cm^{-2}), revealing the more favorable kinetics of Fe_{SA}–N–C (Fig. 4c). The superior performance of Fe_{SA}–N–C to Fe_{NP}–N–C and N–C clearly manifests that single-atom Fe sites are the real origin of the high activity for ORR. It is worth noting that, although much endeavor has been devoted, very limited non-noble metal catalysts were reported to present excellent ORR performance in acidic media. The results highlight the particular superiority of Fe_{SA}–N–C toward ORR among all reported non-noble-metal catalysts (Supplementary Fig. 23, Supplementary Table 8). Given the superb activity of Fe_{SA}–N–C, the deeper ORR investigations have been further conducted in $HClO_4$. To understand the electron transfer mechanism, LSV curves at different rotating rates of rotating disk electrode are recorded. The Koutechy-Levich (K-L) plots obtained from the LSV curves present good linearity, manifesting the first-order reaction kinetics for Fe_{SA}–N–C with a potential-independent electron transfer rate (Supplementary Fig. 24a)[44,45]. The electron transfer number calculated by K-L equation is determined to be 4, in accordance with the result of the rotating ring disk electrode test (Supplementary Fig. 24a, b). Furthermore, the LSV curves of Fe_{SA}–N–C after 20,000 cycles,

and the methanol addition present its excellent durability and methanol tolerance, in stark contrast to the significant decline of Pt/C (Supplementary Figs. 25 and 26). The XPS spectrum of Fe for Fe_{SA}–N–C after stability test shows identical peak to the as-prepared catalyst (Supplementary Fig. 27). From the aberration-corrected HAADF-STEM image, Fe atoms in Fe_{SA}–N–C after stability test still maintain atomic dispersion on the porous carbon (Supplementary Fig. 28). The results above manifest that the single Fe atoms in Fe_{SA}–N–C can retain the structure after stability test. In addition, to ascertain the critical role of single Fe atoms for the excellent ORR, SCN^-, with strong affinity to Fe, was employed to act as a probe to poison Fe–N sites[46,47]. Upon the addition of KSCN solution into 0.1 M $HClO_4$, the deactivation of Fe_{SA}–N–C for ORR, with the half-wave potential decreased significantly by 52 mV, clearly manifests that single Fe atoms are responsible for the excellent ORR performance of Fe_{SA}–N–C (Fig. 4d). The excellent ORR activity in acid media of Fe_{SA}–N–C has been further approved by the PEMFC measurements. The Fe_{SA}–N–C produces a remarkable current density of 292 mA cm^{-2} at 0.8 V (or 463 mA cm^{-2} at 0.8 $V_{iR\text{-}free}$), which is among the highest activities of platinum group metals-free cathodes reported in real PEMFCs (Fig. 4e, Supplementary Fig. 29, Supplementary Table 9). Moreover, the peak power density reaches a considerable value of 0.68 W cm^{-2}, ~54% the power density of the Pt-cathode under the same operating conditions (Fig. 4e). The fuel cell stability test for Fe_{SA}–N–C indicates a stabilized current density ~0.3 A cm^{-2} after 20 h testing at 0.5 V (Supplementary Fig. 30). Furthermore, SiO_2@Fe_{SA}–N–C, featuring much smaller pore size and volume than Fe_{SA}–N–C, has also been tested for fuel cell application (Supplementary Fig. 31). It can be seen that SiO_2@Fe_{SA}–N–C shows much inferior performance to Fe_{SA}–N–C, clearly demonstrating the vital importance of porous structure in Fe_{SA}–N–C for the improvement of fuel cell performance (Supplementary Fig. 32).

To better understand the extraordinary ORR activity of Fe_{SA}–N–C, DFT calculations have been performed to obtain the free energy diagrams of Fe_{SA}–N–C at equilibrium potential based on the four elementary steps of ORR in acidic media (Fig. 4f, Supplementary Figs. 33–35, Supplementary Tables 10–12). It is clear that Fe_{SA}–N–C and Fe_{NP}–N–C show different ORR rate-determining steps. For Fe_{SA}–N–C, the formation of OH* is the most sluggish step with the highest uphill free energy change of 0.55 eV. As for Fe_{NP}–N–C, the rate-determining step is the last electron transfer step, requiring the energy change of 1.25 eV. Obviously, the resistance of ORR on Fe_{SA}–N–C is much smaller than that of Fe_{NP}–N–C, which well explains the outstanding performance of Fe_{SA}–N–C.

Discussion

In summary, we have rationally developed a synthetic strategy toward high-loading SACs by nanocasting SiO_2 into a MOF, PCN-222(Fe). The 3D skeleton of PCN-222(Fe) realizes the spatial isolation of Fe atoms that are bound by the N atoms in the linker. More importantly, the SiO_2 nanocasted in the MOF mesochannels further offers anchoring effect, generating thermally stable FeN_4/SiO_2 interfaces and further inhibiting Fe agglomeration under pyrolysis. By integrating these dual protections, the SiO_2@PCN-222(Fe) composite, as an ideal precursor, affords Fe_{SA}–N–C with a Fe loading (3.46 wt%) higher than almost all reported single-atom Fe in N-doped carbon materials. Moreover, the synthetic approach is readily extendable to other single metal atoms, such as Co_{SA} and Ni_{SA}. Thanks to the high-content Fe_{SA} sites, hierarchical pores and high conductivity of carbon matrix, Fe_{SA}–N–C possesses excellent ORR performance in both alkaline and acidic media, far outperforming all other non-noble-metal catalysts and even the Pt/C. Furthermore, Fe_{SA}–N–C delivers excellent performance in acidic PEMFC, demonstrating the great potential of Fe_{SA}–N–C for PEMFC applications. We believe this nanocasting strategy might open up a fascinating avenue to the general fabrication of SACs with high loadings for broad applications.

Methods

Synthesis of PCN-222(Fe). In a typical experiment, $ZrOCl_2$ (108.6 mg), FeTCPPCl (32 mg), and CF_3COOH (0.45 mL) were dissolved in DMF (10 mL), and ultrasonically dissolved in a 20 mL Pyrex vial. The mixture was heated in 120 °C oven for 18 h. After cooling down to room temperature, the obtained dark brown products were separated by centrifugation, and washed subsequently with DMF for thrice and acetone for twice. The as-obtained precipitates were activated in acetone and finally dried at 60 °C under vacuum overnight.

Synthesis of SiO_2@PCN-222(Fe). Typically, PCN-222(Fe) (30 mg) was transferred to a two-necked flask and degassed for 12 h at 130 °C. When the system was cooled down to room temperature, TEOS (1200 μL) was injected into the flask, and the mixture was sonicated under vacuum for 20 min. Then the obtained solution was centrifuged and the solid was heated at 60 °C under vacuum for 20 min to remove the TEOS on the external surface of the MOF sample. After that, the sample was exposed to 3 M HCl vapor for 9 h at 60 °C to induce the polycondensation of TEOS within the mesopores of the MOF to give SiO_2@PCN-222 (Fe) composite.

Synthesis of Fe_{SA}–N–C. Typically, SiO_2@PCN-222(Fe) was heated from the room temperature to 800 °C with a heating rate of 5 °C min^{-1}, then maintained at this temperature for 2 h in N_2 atmosphere. The metal oxides were removed by immersing the sample in the HF (20 wt%) solution for 6 h at 80 °C (Caution! HF is highly toxic and should be handled very carefully). The black sample was collected by centrifuging, washed several times with distilled water and ethanol, and dried at 60 °C under vacuum overnight.

Synthesis of Fe_{NP}–N–C. Typically, Fe_{NP}–N–C was obtained from the direct pyrolysis of pure PCN-222(Fe) following the same procedure as Fe_{SA}–N–C.

Data availability

The data that support the findings of this study are available from the corresponding author upon reasonable request.

Received: 7 August 2019; Accepted: 13 May 2020;
Published online: 05 June 2020

References

1. Yang, X.-F. et al. Single-atom catalysts: a new frontier in heterogeneous catalysis. *Acc. Chem. Res.* **46**, 1740–1748 (2013).
2. Liu, J. Catalysis by supported single metal atoms. *ACS Catal.* **7**, 34–59 (2017).
3. Zhu, C., Fu, S., Shi, Q., Du, D. & Lin, Y. Single-atom electrocatalysts. *Angew. Chem. Int. Ed.* **56**, 13944–13960 (2017).
4. Zhang, H., Liu, G., Shi, L. & Ye, J. Single-atom catalysts: emerging multifunctional materials in heterogeneous catalysis. *Adv. Energy Mater.* **8**, 1701343 (2018).
5. Liu, L. & Corma, A. Metal catalysts for heterogeneous catalysis: from single atoms to nanoclusters and nanoparticles. *Chem. Rev.* **118**, 4981–5079 (2018).
6. Xu, H., Cheng, D., Cao, D. & Zeng, X. C. A universal principle for a rational design of single-atom electrocatalysts. *Nat. Catal.* **1**, 339–348 (2018).
7. Zhang, H. et al. Dynamic traction of lattice-confined platinum atoms into mesoporous carbon matrix for hydrogen evolution reaction. *Sci. Adv.* **4**, eaao6657 (2018).
8. Gu, J., Hsu, C., Bai, L., Chen, H. & Hu, X. Atomically dispersed Fe^{3+} sites catalyze efficient CO_2 electroreduction to CO. *Science* **364**, 1091–1094 (2019).
9. Chen, Y. et al. Single-atom catalysts: synthetic strategies and electrochemical applications. *Joule* **2**, 1242–1264 (2018).
10. Zhang, L. et al. Graphene defects trap atomic Ni species for hydrogen and oxygen evolution reactions. *Chem* **4**, 285–297 (2018).
11. Liu, P. et al. Photochemical route for synthesizing atomically dispersed palladium catalysts. *Science* **352**, 797–800 (2016).
12. Hülsey, M. J., Zhang, J. & Yan, N. Harnessing the wisdom in colloidal chemistry to make stable single-atom catalysts. *Adv. Mater.* **30**, 1802304 (2018).

13. Yin, P. et al. Single cobalt atoms with precise N-coordination as superior oxygen reduction reaction catalysts. *Angew. Chem. Int. Ed.* **55**, 10800–10805 (2016).
14. Sun, X. et al. Single cobalt sites in mesoporous N-doped carbon matrix for selective catalytic hydrogenation of nitroarenes. *J. Catal.* **357**, 20–28 (2018).
15. Chen, Y.-Z., Zhang, R., Jiao, L. & Jiang, H.-L. Metal-organic framework-derived porous materials for catalysis. *Coord. Chem. Rev.* **362**, 1–23 (2018).
16. Zhang, J., Chen, G., Müllen, K. & Feng, X. Carbon-rich nanomaterials: fascinating hydrogen and oxygen electrocatalysts. *Adv. Mater.* **30**, 1800528 (2018).
17. Furukawa, H., Cordova, K. E., O'Keeffe, M. & Yaghi, O. M. The chemistry and applications of metal-organic frameworks. *Science* **341**, 1230444 (2013).
18. Zhou, H.-C. & Kitagawa, S. Metal-organic frameworks (MOFs). *Chem. Soc. Rev.* **43**, 5415–5418 (2014).
19. Ma, T. Y., Dai, S., Jaroniec, M. & Qiao, S. Z. Metal-organic framework derived hybrid Co_3O_4-carbon porous nanowire arrays as reversible oxygen evolution electrodes. *J. Am. Chem. Soc.* **136**, 13925–13931 (2014).
20. Li, B. et al. Emerging multifunctional metal–organic framework materials. *Adv. Mater.* **28**, 8819–8860 (2016).
21. Islamoglu, T. et al. Postsynthetic tuning of metal-organic frameworks for targeted applications. *Acc. Chem. Res.* **50**, 805–813 (2017).
22. Jiao, L., Wang, Y., Jiang, H.-L. & Xu, Q. Metal-organic frameworks as platforms for catalytic applications. *Adv. Mater.* **30**, 1703663 (2018).
23. Wang, Y.-R. et al. Oriented electron transmission in polyoxometalate-metalloporphyrin organic framework for highly selective electroreduction of CO_2. *Nat. Commun.* **9**, 4466 (2018).
24. Li, G., Zhao, S., Zhang, Y. & Tang, Z. Metal-organic frameworks encapsulating active nanoparticles as emerging composites for catalysis: recent progress and perspectives. *Adv. Mater.* **30**, 1800702 (2018).
25. Zhao, X., Wang, Y., Li, D.-S., Bu, X. & Feng, P. Metal–organic frameworks for separation. *Adv. Mater.* **30**, 1705189 (2018).
26. Jiao, L. & Jiang, H.-L. Metal-organic-framework-based single-atom catalysts for energy applications. *Chem* **5**, 786–804 (2019).
27. Jiao, L. et al. From metal–organic frameworks to single-atom Fe implanted N-doped porous carbons: efficient oxygen reduction in both alkaline and acidic media. *Angew. Chem. Int. Ed.* **57**, 8525–8529 (2018).
28. Zhang, H. et al. Single atomic iron catalysts for oxygen reduction in acidic media: particle size control and thermal activation. *J. Am. Chem. Soc.* **139**, 14143–14149 (2017).
29. Ye, Y. et al. Surface functionalization of ZIF-8 with ammonium ferric citrate toward high exposure of Fe-N active sites for efficient oxygen and carbon dioxide electroreduction. *Nano Energy* **38**, 281–289 (2017).
30. Jiang, R. et al. Edge-site engineering of atomically dispersed Fe-N_4 by selective C-N bond cleavage for enhanced oxygen reduction reaction activities. *J. Am. Chem. Soc.* **140**, 11594–11598 (2018).
31. Wan, X. et al. Fe-N-C electrocatalyst with dense active sites and efficient mass transport for high-performance proton exchange membrane fuel cells. *Nat. Catal.* **2**, 259–268 (2019).
32. Chen, Y. et al. Isolated single iron atoms anchored on N-doped porous carbon as an efficient electrocatalyst for the oxygen reduction reaction. *Angew. Chem. Int. Ed.* **56**, 6937–6941 (2017).
33. Abdel-Mageed, A. M. et al. Highly active and stable single-atom Cu catalysts supported by a metal–organic framework. *J. Am. Chem. Soc.* **141**, 5201–5210 (2019).
34. Zhang, X. et al. Silica-protected ultrathin Ni_3FeN nanocatalyst for the efficient hydrolytic dehydrogenation of NH_3BH_3. *Adv. Energy Mater.* **8**, 1702780 (2018).
35. Kang, X. et al. Synthesis of supported ultrafine non-noble subnanometer-scale metal particles derived from metal-organic frameworks as highly efficient heterogeneous catalysts. *Angew. Chem. Int. Ed.* **55**, 1080–1084 (2016).
36. Wang, Q. et al. Structural evolution of solid Pt nanoparticles to a hollow PtFe alloy with a Pt-skin surface via space-confined pyrolysis and the nanoscale kirkendall effect. *Adv. Mater.* **28**, 10673–10678 (2016).
37. Malonzo, C. D. et al. Thermal stabilization of metal-organic framework-derived single-site catalytic clusters through nanocasting. *J. Am. Chem. Soc.* **138**, 2739–2748 (2016).
38. Sa, Y. J. et al. A general approach to preferential formation of active Fe-N_x sites in Fe-N/C electrocatalysts for efficient oxygen reduction reaction. *J. Am. Chem. Soc.* **138**, 15046–15056 (2016).
39. Feng, D. et al. Zirconium-metalloporphyrin PCN-222: mesoporous metal-organic frameworks with ultrahigh stability as biomimetic catalysts. *Angew. Chem. Int. Ed.* **51**, 10307–10310 (2012).
40. Morris, W. et al. Synthesis, structure, and metalation of two new highly porous zirconium metal-organic frameworks. *Inorg. Chem.* **51**, 6443–6445 (2012).
41. Chen, Y., Hoang, T. & Ma, S. Biomimetic catalysis of a porous iron-based metal-metalloporphyrin framework. *Inorg. Chem.* **51**, 12600–12602 (2012).
42. Liang, H. W., Zhuang, X., Brüller, S., Feng, X. & Müllen, K. Hierarchically porous carbons with optimized nitrogen doping as highly active electrocatalysts for oxygen reduction. *Nat. Commun.* **5**, 4973 (2014).
43. Zhang, Z., Sun, J., Wang, F. & Dai, L. Efficient oxygen reduction reaction (ORR) catalysts based on single iron atoms dispersed on a hierarchically structured porous carbon framework. *Angew. Chem. Int. Ed.* **57**, 9038–9043 (2018).
44. Meng, J. et al. General oriented formation of carbon nanotubes from metal–organic frameworks. *J. Am. Chem. Soc.* **139**, 8212–8221 (2017).
45. Liang, Y. et al. Covalent hybrid of spinel manganese-cobalt oxide and graphene as advanced oxygen reduction electrocatalysts. *J. Am. Chem. Soc.* **134**, 3517–3523 (2012).
46. Jiang, W.-J. et al. Understanding the high activity of Fe-N-C electrocatalysts in oxygen reduction: Fe/Fe_3C nanoparticles boost the activity of Fe-N_x. *J. Am. Chem. Soc.* **138**, 3570–3578 (2016).
47. Wang, Q. et al. Phenylenediamine-based FeN_x/C catalyst with high activity for oxygen reduction in acid medium and its active-site probing. *J. Am. Chem. Soc.* **136**, 10882–10885 (2014).

Acknowledgements

L.J., R.Z., and G.W. contributed equally to this work. This work is supported by the NSFC (21725101, 21871244, 21673213, and 21521001), China Postdoctoral Science Foundation (2019TQ0298 and 2019M660151), International Partnership Program of CAS (211134KYSB20190109), Fundamental Research Funds for the Central Universities (WK2060030029), BSRF, SSRF, National Synchrotron Radiation Laboratory Foundation (KY2060000160) and Fujian Institute of Innovation (CAS). Use of the Advanced Photon Source is supported by the U.S. Department of Energy, Office of Science, Office of Basic Energy Sciences, under Contract No. DE-AC02-06CH11357, and the Canadian Light Source and its funding partners. The calculations in this work are supported by the supercomputing system in the Supercomputing Center of University of Science and Technology of China.

Author contributions

H.-L.J. conceived the idea and supervised the project. L.J. and R.Z. performed the experiments, characterizations, and electrochemical measurements. G.W. and H.Z. performed the X-ray absorption spectroscopy measurements and analyses. W.Y. performed the theoretical calculations. X.W. and J.S. performed the fuel cell measurements. H.-L.J. and L.J. analyzed the data and co-wrote the paper. H.Z., J.S., and S.-H.Y. discussed the results and commented the manuscript.

Competing interests

The authors declare no competing interests.

Additional information

Supplementary information is available for this paper at https://doi.org/10.1038/s41467-020-16715-6.

Correspondence and requests for materials should be addressed to H.-L.J.

Peer review information *Nature Communications* thanks the anonymous reviewer(s) for their contribution to the peer review of this work.

Reprints and permission information is available at http://www.nature.com/reprints

Publisher's note Springer Nature remains neutral with regard to jurisdictional claims in published maps and institutional affiliations.